



# An elastic, low-background vertical focusing element for a doubly focusing neutron monochromator<sup>☆</sup>

Stephen A. Smee<sup>a,b,\*</sup>, Paul C. Brand<sup>b</sup>, Dwight D. Barry<sup>b</sup>, Collin L. Broholm<sup>c,b</sup>,  
Dave K. Anand<sup>a</sup>

<sup>a</sup>Department of Mechanical Engineering, University of Maryland, College Park, MD 20742, USA

<sup>b</sup>National Institute of Standards and Technology, Gaithersburg, MD 20899, USA

<sup>c</sup>Department of Physics and Astronomy, The Johns Hopkins University, Baltimore, MD 21218, USA

Received 23 January 2001

## Abstract

A novel, variable radius of curvature, device for the focusing of neutrons is presented. This elastic element consists of a thin variable thickness, constant width, aluminum blade to which diffracting crystals can be attached. When buckled, the blade assumes a circular focal shape, the radius of which is easily controlled by the relative displacement of supporting pivots. Precision electromechanical and optical measurements show that the slope of the buckled blade conforms to a circular arc to within 0.15° for radii in the range 900 mm <  $R$  < 10 000 mm. This easily scalable, low mass mechanism is well suited for use in a focusing neutron monochromator, as the parasitic scattering typically associated with traditional lead screw and lever mechanisms is greatly reduced. © 2001 Elsevier Science B.V. All rights reserved.

**Keywords:** Neutron monochromator; Neutron spectrometer; Doubly focusing; Neutron scattering; Vertical focusing

## 1. Introduction

Neutron spectroscopy is widely used in material science and condensed matter physics to probe structure and dynamics of materials. Often, the ability to obtain information from a scattering

experiment is limited by the neutron flux at the sample. As a result, much has been done in recent years to design beam delivery systems that make optimal use of the source of neutrons without sacrificing required resolution. Most instruments at reactor neutron sources rely on Bragg reflection to reflect a monochromatic beam from the moderator to the sample. Riste was the first to suggest that Bragg reflection also be used to focus the diverging beam from the source onto the sample and thereby increase the flux [1]. Early devices focused in the vertical plane only thus maintaining good angular resolution in the horizontal plane. When angular resolution can be further relaxed as is the case, for example, in experiments using long wavelength neutrons, the technique can be generalized to encompass

<sup>☆</sup>Certain commercial equipment, instruments, or materials are identified in this paper in order to specify the experimental procedure adequately. Such identification is not intended to imply recommendation or endorsement by the National Institute of Standards and Technology, nor is it intended to imply that the materials or equipment identified are necessarily the best available for the purpose.

\*Corresponding author. Department of Mechanical Engineering, University of Maryland, College Park, MD 20742 USA. Tel.: +1-410-516-7080.

E-mail address: smee@eng.umd.edu (S.A. Smee).

focusing in both the vertical and horizontal plane. The combination of vertical and horizontal focusing provides a significant increase in flux over flat single crystal monochromators, with an acceptable loss in wave vector resolution for long wavelength neutrons or in experiments where wave vector resolution is not required [2]. Doubly focusing monochromators are now being used successfully on several neutron scattering spectrometers around the world.

While the monochromatic flux at the sample position is important for neutron scattering studies, ultimately it is the signal to noise at the detector that is the metric of interest, especially when working with small samples. From the perspective of the monochromator, maximum signal to noise is achieved by maximizing the solid angle subtended to the source while minimizing the noise, or *background*, produced. Both these considerations are affected by the monochromator design, the former being affected by the size of the array and the latter by the amount of structural material in the beam. Therefore, for a doubly focusing monochromator that utilizes an array of single crystals, the goal is to maximize the area of the array while minimizing the structural material used to position the crystals.

One of the problems with the doubly focusing technique is the mechanical complexity required to optimize focusing for a range of incident energies. This stems from the fact that Bragg's law requires different scattering angles for different incident energies, which in turn implies that the radii of curvature must change with energy. This complexity has ultimately led to complex focusing mechanisms. Presently, most doubly focusing monochromators employ intricate mechanical mechanisms to orient each crystal in the array at the proper focusing angle. The type of mechanism traditionally used is the lead-screw and lever [3,4]. In such a design, each crystal in a column of the array is mounted on a platelet whose tilt is controlled by a lead-screw driven lever. Lead-screw rotation adjusts the tilt of each crystal placing them tangent to an arc of constant radius thus providing vertical focus. By rotating each column to the desired Bragg angle, horizontal focus is achieved. The problem with this type of

mechanism is twofold: (i) The mass of the focusing mechanism is much greater than that of the crystal and it is constructed using materials that often have high scattering cross sections; this ultimately leads to a significant level of background. (ii) The complexity of the mechanism limits both the size and number of crystals that can be realistically implemented. For spectroscopic systems requiring high signal to noise, this type of focusing mechanism is undesirable.

In this paper, a novel vertical focusing device that overcomes the fundamental limitations of its predecessors is presented. This low-background variable-curvature vertical focusing element consists of a thin, variable thickness, constant width, aluminum blade that, when buckled, assumes the shape of an arc of constant radius over a wide range of radii. When populated with a one-dimensional array of diffracting crystals, this scalable, low mass device is ideally suited to vertically focus neutrons especially as part of an actively controlled doubly focusing neutron monochromator. The technique is related to that proposed and implemented by Popovici et al. [5] where focusing is achieved by directly deforming the Bragg reflecting single crystal. The technique proposed here enables focusing without lead-screws and levers in the beam when the size and elastic properties of the single crystalline material precludes direct deformation.

## 2. Blade design

The use of elastically deformable elements in precision instrumentation is a common practice. Flexures, a class of such devices, are often used in motion control applications where high resolution, zero-backlash motion is required. Here the concept is applied to vertically focusing neutrons, see Fig. 1. The device shown consists, simply, of a thin elastic blade supported at each end by pivots. Mounted to the blade is a one-dimensional array of crystals. By controlling the relative displacement of the pivots,  $\delta x$ , the blade buckles forming the shape of an arc thus focusing neutrons emanating from a source onto a sample.

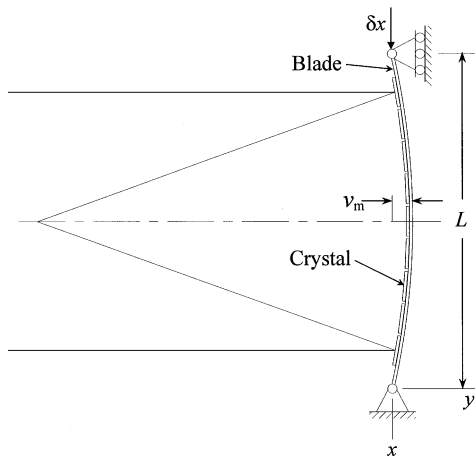


Fig. 1. Conceptual sketch of an elastic, variable curvature focusing element. Crystals are attached to the concave side of a thin blade, which assumes the shape of an arc when buckled. The radius of curvature is controlled by changing the pivot-to-pivot distance,  $L$ .

The advantages of such a device are clear. It is simple and easily scalable thus it facilitates the construction of large arrays containing hundreds of individual crystals. Backlash, typical of lead-screw driven mechanisms, is nonexistent. And, most importantly, parasitic scattering is minimized due to the very low mass design and the monolithic nature of the device, which eliminates the need for highly scattering materials in the beam. The challenge with such a device is achieving, within a high degree of accuracy, the proper focal surface over a wide range of radii through the control of a single degree of freedom, the pivot displacement  $\delta x$ . The solution to this difficulty is the thrust of the work presented here.

The ideal curvature for a vertically focusing device used in typical spectroscopic configurations is elliptical, see Fig. 2. However, a circular curvature is used here because it closely approximates an ellipse for the spectroscopic configuration under development, and it is easier to control since it only requires the adjustment of a single degree of freedom, the radius. This simplification is often made when designing vertically focusing monochromators. Therefore, the objective is to design the blade in such a way that it buckles into an arc of constant radius over a specified focal range. The application leading to this work calls

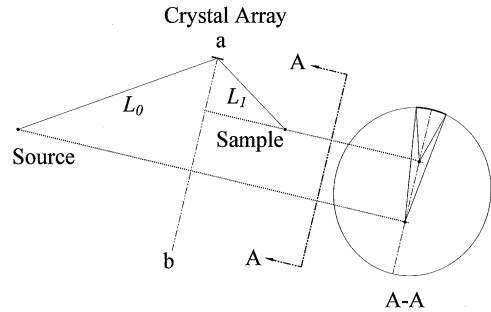


Fig. 2. Layout of a typical vertically focusing monochromator. The projection of  $L_0$  and  $L_1$  onto  $\overline{ab}$  shows that, for  $L_0 \neq L_1$ , the ideal focal surface is elliptical, see inset A-A.

for radii in the range  $900 \text{ mm} < R < 10\,000 \text{ mm}$  [2]. Additionally, the slope angle of the blade should not deviate from the desired shape by more than a fraction of the crystal mosaicity for optimum performance. The tolerable deviation set for this work is  $\sim 0.15^\circ$ , leading to a 10% increase in the effective mosaicity of the array as compared to the mosaicity of an individual crystal.

### 2.1. Prismatic blade

The simplest blade to construct and analyze is one with a constant cross-section. In beam theory the term used for this type of geometry is *prismatic* and, as a point of reference, it is instructive to examine the focal performance of this simple case.

For a prismatic beam subject to an applied axial load, closed-form expressions for the buckled shape exist for a variety of boundary conditions. The condition of interest here is the pinned–pinned scenario depicted in Fig. 1. The deflection curve,  $v(x)$ , for this condition is given by [6]

$$v(x) = v_m \sin\left(\frac{\pi x}{L}\right) \quad (1)$$

where  $v_m$  is the deflection at the center of the beam and  $L$  is the distance between the pinned ends. (For a list of symbols and their explanations and units, see Table 1.)

The slope, which defines the orientation of the crystal mounting surface, is simply the derivative of Eq. (1), or

$$v'(x) = \frac{\pi}{L} v_m \cos\left(\frac{\pi x}{L}\right) \quad (2)$$

Table 1

List of symbols with short explanations and units

Symbol	Description	Units
$L$	Pivot-to-pivot distance	mm
$\delta x$	Pivot displacement	mm
$v(\xi)$	Deflection of buckled blade, $\xi = x$ or $s$	mm
$v'(\xi)$	Slope of deflection curve, $\xi = x$ or $s$	rad
$v_m$	Maximum deflection of buckled blade	mm
$w(x)$	Deflection of a circular deflection curve	mm
$w'(x)$	Slope of a circular deflection curve	rad
$w_m$	Maximum deflection of a circular deflection curve	mm
$\Phi$	Slope angle of deflection curve	deg
$R$	Radius of curvature of buckled blade	mm
$L_0$	Distance from source to monochromator	mm
$L_1$	Distance from monochromator to sample	mm
$\varepsilon_v(R, \xi)$	Vertical aberration, i.e. slope error, $\xi = x$ or $s$	deg
$\varepsilon_h(R, \xi)$	Horizontal aberration, $\xi = x$ or $s$	deg
$M$	Moment	N mm
$F(R)$	Buckling force	N
$I(\xi)$	Moment of inertia, $\xi = x$ or $s$	mm <sup>4</sup>
$E$	Modulus of elasticity	Pa
$b(s)$	Blade width	mm
$b_m$	Maximum blade width	mm
$t(s)$	Blade thickness	mm
$t_m$	Maximum blade thickness	mm
$h$	Minimum blade thickness	mm
$k_1$	Knuckle length	mm
$k_t$	Knuckle thickness	mm
$S$	Blade half-length	mm
$\tau(s)$	Shale function describing the blade thickness profile	mm
$\delta_e(s)$	Offset function describing the location of the neutral surface	mm
$\beta$	Location where $t(s) = h$	mm

and is the metric of interest for determining the focal performance of the device. The desire here is to match, as closely as possible, the slope of a circular arc, which is given by

$$w'(x) = \frac{L/2 - x}{\sqrt{((L^2 + 4w_m^2)/8w_m)^2 - (L/2 - x)^2}} \quad (3)$$

corresponding to a radius of curvature

$$R = \frac{L^2 + 4w_m^2}{8w_m}. \quad (4)$$

The focal performance is quantified by taking the difference in slope angle between the desired

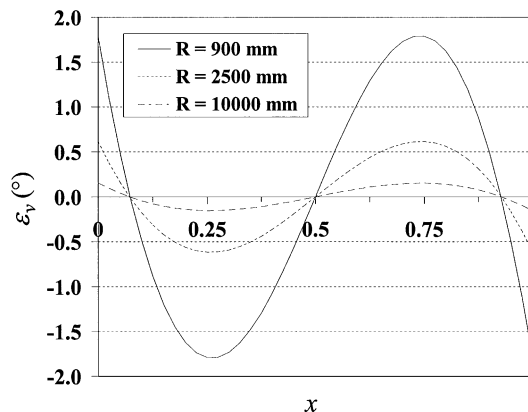


Fig. 3. Vertical aberration in a buckled pinned–pinned blade of constant cross-section. Deflections are normalized with respect to the pivot distance,  $L$ .

deflection curve (circular) and the actual deflection curve (sinusoidal in this case). This *slope error* is defined as the vertical aberration and is given by

$$\varepsilon_v(x) = \text{atan}(w'(x)) - \text{atan}(v'(x)). \quad (5)$$

Fig. 3 shows  $\varepsilon_v$  as a function of normalized length for three curvatures in the focal range  $900 \text{ mm} < R < 10\,000 \text{ mm}$ . As shown in the plot, the aberration is a function of radius and the magnitude increases with increasing curvature. It is obvious that, except for very large radii, the aberration in a prismatic blade is significant compared to the mosaicity of most diffracting crystals of interest and is considerably larger than the  $0.15^\circ$  requirement for this work.

## 2.2. Non-prismatic blade

From the results presented above, it is evident that the slope error resulting from use of a constant cross-section blade is significant. However, the error can be reduced considerably if the cross-section of the blade is varied with length, i.e. if the blade is non-prismatic. In this section, the non-prismatic geometry is derived for a blade that assumes the proper circular shape when buckled. For this development, the curvilinear coordinate of the blade axis, defined by the deflection curve, is used as the independent variable since it is the shape of the blade with respect to this coordinate that is of interest.

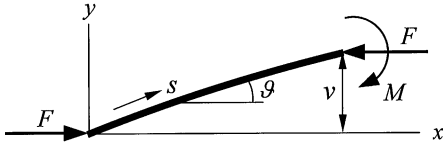


Fig. 4. Free-body diagram for pinned–pinned buckled beam.

The governing differential equation for the deflection of an elastic beam is [6]

$$\frac{d\vartheta}{ds} = -\frac{M}{EI} \quad (6)$$

and the free-body diagram for the problem here is shown in Fig. 4. Eq. (6), states simply that the curvature at a point along the deflection curve is equal to the moment,  $M$ , divided by the bending stiffness  $EI$ , where  $E$  is the modulus of elasticity and  $I$  is the moment of inertia; the negative sign is an artifact of sign convention.

For this loading condition,  $M = Fv$ , with  $F$  being the force and  $v$  the transverse displacement. Substituting this expression for the moment and recognizing that the curvature,  $d\vartheta/ds$ , is constant for the circular deflection profile, the governing equation, Eq. (6), simplifies to

$$\frac{v(s)}{I} = -\frac{E}{FR} \quad (7)$$

after some rearrangement. Since the transverse displacement,  $v$ , is a function of  $s$  and the right hand side of Eq. (7) is constant, the equality can only be satisfied if the geometric variable, the moment of inertia,  $I$ , is a function of  $s$  as well. Therefore, the blade must be non-prismatic if it is to buckle to the desired circular shape.

The proper geometry, or *shape function*, of the variable moment of inertia blade can easily be obtained from the derivative of Eq. (6). Rearranging terms and taking the derivative we have

$$\frac{d^2\vartheta}{ds^2} + \left(\frac{F}{E}\right) \frac{d}{ds} \left(\frac{v}{I}\right) = 0. \quad (8)$$

Expanding the first derivative term and taking into account the fact that the derivative of the curvature is zero for a circular deflection profile leads to

$$\frac{dv}{ds} - \frac{v}{I} \frac{dI}{ds} = 0. \quad (9)$$

Multiplying through by  $ds$ , separating variables and integrating yields the solution

$$\ln(I) = \ln(v) + C_1 \quad (10)$$

or simply

$$I = C_2 v \quad (11)$$

where the deflection curve,  $v(s)$ , for a circular arc is given by

$$v(s) = R \left( \cos\left(\frac{S-s}{R}\right) - \cos\left(\frac{S}{R}\right) \right). \quad (12)$$

Here,  $S$  is the half-length of the blade.

The constant  $C_2$  is determined from the condition

$$I(S) = C_2 v(S). \quad (13)$$

Given the symmetry of the blade,  $I_m = I(S)$ , and

$$C_2 = \frac{I_m}{R(1 - \cos(S/R))}. \quad (14)$$

Substituting Eqs. (12) and (14) into Eq. (11) yields the moment of inertia as a function of  $s$ ,

$$I(s) = I_m \left( \frac{\cos((S-s)/R) - \cos(S/R)}{1 - \cos(S/R)} \right), \quad 0 < s < 2S. \quad (15)$$

For a beam of rectangular cross-section with a width,  $b$ , and a thickness,  $t$ , the moment of inertia is

$$I = \frac{bt^3}{12}. \quad (16)$$

From Eqs. (15) and (16), two alternatives for the shape function are easily obtained, they are:

*Variable width—constant thickness:*

$$b(s) = b_m \left( \frac{\cos((S-s)/R) - \cos(S/R)}{1 - \cos(S/R)} \right), \quad 0 < s < 2S. \quad (17)$$

*Variable thickness—constant width:*

$$t(s) = t_m \sqrt[3]{\frac{\cos((S-s)/R) - \cos(S/R)}{1 - \cos(S/R)}}, \quad 0 < s < 2S. \quad (18)$$

It is evident from Eqs. (17) and (18) that the width and thickness, respectively, tend to zero as  $s \rightarrow 0$ . From a practical perspective, a tapered width is much less desirable than a tapered thickness since the surface area for mounting crystals and the torsional stiffness is reduced significantly by the former. For this reason, only the variable thickness option, Eq. (18), will be considered here.

Further inspection of Eq. (18) reveals that  $t(s)$  is independent of  $R$  to second order and for  $R \gg S$  the shape function is virtually independent of  $R$ . In fact, regardless of the value chosen within the range  $900 \text{ mm} < R < 10\,000 \text{ mm}$ , the maximum variation in thickness over the length of the blade is 0.15%. The significance of this cannot be overstated. Specifically, it implies that it is possible to construct a blade of fixed dimension that will bend into an arc of constant radius over a wide range of radii.

### 2.3. Design details

There are several practical design considerations that influence the geometry of the blade. First, the need to integrate pivot hardware and difficulties in fabrication require that a minimum thickness,  $h$ , at the ends of the blade be defined; the zero thickness defined by the shape function, Eq. (18) is impractical. The minimum thickness should be chosen so that only a small fraction of the blade deviates from the desired shape. Second, to facilitate the implementation of pivot hardware—a vee-jewel is used here—the thickness in a short region at the ends of the blade must be increased considerably; this region is referred to here as the *knuckle*. As with the length of the minimum thickness region, the length of the knuckle should be minimized. Third, it is desirable, for crystal mounting purposes, to make one surface of the blade flat while the other assumes the profile given by Eq. (18). The crystals are mounted to the flat surface, which, when buckled, conforms to the desired circular profile. This asymmetric condition has an additional benefit in that it leads naturally to an eccentric buckling load, which guarantees that buckling is always concave on the crystal side. These considerations, and Eq. (18), are integrated

in the blade design presented here, which is illustrated in Fig. 5.

The unbuckled blade length, from pivot to pivot, is 440 mm, the width,  $b$ , is 19 mm, and the central thickness,  $t_m$ , is 2 mm. The minimum thickness,  $h$ , is 0.887 mm and the knuckle dimensions are:  $k_t = 6.35 \text{ mm}$  and  $k_l = 8.75 \text{ mm}$ . The blade accommodates up to nineteen  $20 \text{ mm} \times 20 \text{ mm} \times 2 \text{ mm}$  crystals. Small threaded holes in the blade are used to fasten the crystals, two screws per crystal, and an aluminum shim,  $19 \text{ mm} \times 5 \text{ mm} \times 0.25 \text{ mm}$ , resides between each crystal and the blade to avoid straining the crystals as the blade is deflected. The material selected here is 6061-T6 aluminum. This alloy is easy to machine, has high fatigue strength, and a low scattering cross-section. It should be noted that, while other aluminum alloys have higher strength, these alloys contain activating elements and are less desirable. The mass of the blade is 43 g.

## 3. Numerical analysis

### 3.1. Model geometry

A simplified version of the geometry depicted in Fig. 5 has been modeled numerically to predict the focal performance of the non-prismatic blade. This simplified representation is shown in the free-body diagram, Fig. 6. For this study, the width is

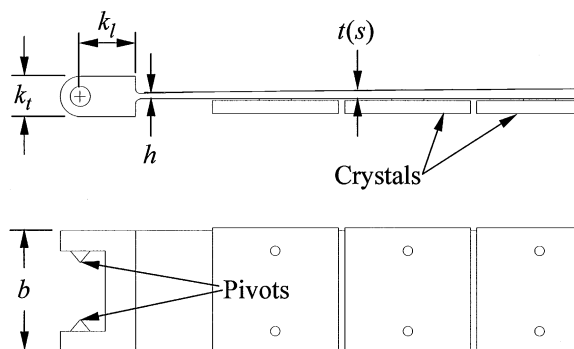


Fig. 5. Blade design details. Crystals mount to the flat surface of the blade. Opposing, pointed screws preloaded into sapphire conical sockets establish the pivot.

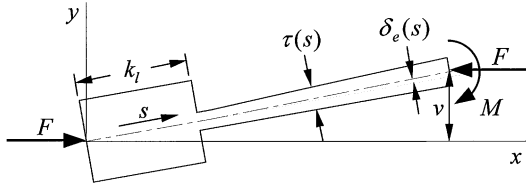


Fig. 6. Free-body diagram of the variable thickness blade.

assumed constant throughout; the threaded holes and notch in the knuckle are ignored. The blade is modeled from the pivot point to the plane of symmetry at the half-length,  $s = S$ , and the neutral surface is taken to be at the half-thickness of the blade, the location of which is defined by the offset function,  $\delta_e$ . The thickness profile,  $\tau(s)$ , modeled here is

$$\tau(s) = \begin{cases} k_1, & 0 \leq s \leq k_1 \\ h, & k_1 < s < \beta \\ t(s), & \beta \leq s \leq S \end{cases} \quad (19)$$

and the offset function  $\delta_e(s)$  is given by

$$\delta_e(s) = \begin{cases} 0, & 0 \leq s < \beta \\ \frac{t(s) - h}{2}, & \beta \leq s \leq S \end{cases} \quad (20)$$

where  $\beta$  is defined by  $t(\beta) = h$  using Eq. 18. For the purpose of defining  $t(s)$ , the radius,  $R$ , used here was 900 mm. The geometric parameters relevant to this study are

$$k_1 = 6.35 \text{ mm} \quad (21)$$

$$k_1 = 8.75 \text{ mm} \quad (22)$$

$$h = 0.887 \text{ mm} \quad (23)$$

$$S = 220 \text{ mm} \quad (24)$$

$$t_m = 2 \text{ mm} \quad (25)$$

$$b = 19 \text{ mm}. \quad (26)$$

### 3.2. Mathematical formulation

To accurately predict the deflection curve of the buckled blade, the exact governing equation for the deflection of a beam, Eq. (6), is utilized. The dependent variable has been changed to express the equation in terms of the transverse displace-

ment,  $v$ , as opposed to the slope angle,  $\vartheta$ . Specifically,

$$\frac{d^2v}{ds^2} = -\frac{M}{EI} \left( 1 - \left( \frac{dv}{ds} \right)^2 \right)^{1/2} \quad (27)$$

where the substitution,

$$\frac{d\vartheta}{ds} = \frac{d^2v/ds^2}{\left( 1 - (dv/ds)^2 \right)^{1/2}} \quad (28)$$

facilitates the change in variable. Rearranging terms in Eq. (27) and recognizing, from Fig. 6, that  $M = F(v + \delta_e)$ , yields the equation of interest:

$$\frac{d^2v}{ds^2} + \frac{F}{EI}(v + \delta_e) \left( 1 - \left( \frac{dv}{ds} \right)^2 \right)^{1/2} = 0 \quad (29)$$

where

$$I = \frac{b\tau^3}{12} \quad (30)$$

subject to the boundary conditions

$$v(0) = 0 \quad (31)$$

$$\left. \frac{dv}{ds} \right|_{s=S} = 0. \quad (32)$$

Computationally, the solution to Eq. (29) becomes tractable if the differential equation is separated into a system of first-order equations that can be integrated numerically, specifically,

$$z_0 = v \quad (33)$$

$$\frac{dz_0}{ds} = z_1 \quad (34)$$

$$\frac{dz_1}{ds} = -\frac{F}{EI}(z_0 + \delta_e)(1 - z_1^2)^{1/2}. \quad (35)$$

Note that the effect of crystal mounting is not considered in the above formulation. This is due to uncertainty in the degree of shear transfer across the crystal/shim/blade interfaces. Rather than trying to predict the effect mathematically, the influence of crystal mounting is characterized experimentally.

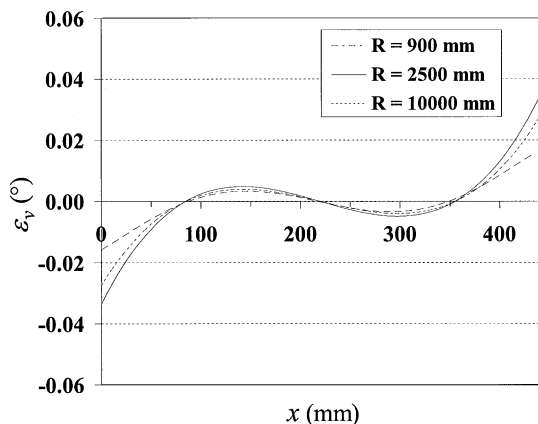


Fig. 7. Vertical aberration for a variable thickness blade. The aberration is plotted for three radii:  $R=900$ , 2500 and 10000 mm.

### 3.3. Numerical results

Eqs. (34) and (35) were discretized over the domain  $0 \leq s \leq S$  and solved numerically, subject to the boundary conditions, Eqs. (31) and (32), using a fourth-order Runge–Kutta scheme. The force,  $F$ , was solved for iteratively by adhering to the boundary condition, Eq. (32). The grid consisted of 1280 equally spaced intervals and was determined, through mesh refinement studies, to provide grid independent results. For this study, the modulus of elasticity,  $E$ , for aluminum was taken to be 70 Gpa.

From the numerical results, the maximum buckling load was determined to be 36 N ( $R=900$  mm) and the corresponding bending stress is 77 MPa, below the endurance limit of 97 MPa for 6061-T6 aluminum [7]<sup>1</sup>. For this stress level and low-frequency applications of the device, infinite fatigue-life can be expected.

Deflection profiles were calculated for  $900 \leq R \leq 10000$  mm and the vertical aberration,  $\varepsilon_v$ , for three radii in this range, is shown in Fig. 7; the curve  $R=2500$  mm being the worst case. The data shows that the vertical aberration in the variable thickness blade is significantly less than in a prismatic blade. By varying the thickness,  $\varepsilon_v$  has been reduced from more than  $1.5^\circ$  to less than

$0.05^\circ$  on a theoretical basis, a value that is negligible compared to the mosaicity of many crystals of interest. It is also evident that  $\varepsilon_v$  is virtually independent of radius; thus, confirming the theoretical prediction which stems from the mathematical formulation of the shape function.

To predict the effect of geometric inaccuracies resulting from the manufacturing process, several numerical studies were conducted. These studies modeled the effects of simple symmetric variations in geometry. The variables perturbed were the blade thickness and the location of the pivots, specifically, the position of the pivots with respect to the neutral surface and the distance between the pivots. In each case, the amount of variance corresponds to a reasonable manufacturing tolerance.

Figs. 8a and b show  $\varepsilon_v$  for a blade with a uniform  $\pm 12 \mu\text{m}$  offset of the shape function buckled to  $R=900$  and 10000 mm, respectively. Fig. 8a shows that the functional form of the slope error curve for  $R=900$  mm is highly sensitive to small variances in blade thickness, particularly near the ends of the blade. For  $R=10000$  mm, the effect of this geometric variance is minimal, as is evident from Fig. 8b. In either case, the maximum slope error is still well below  $0.15^\circ$ .

Figs. 9a and b show  $\varepsilon_v$  for a blade with a  $\pm 50 \mu\text{m}$  deviation in the location of the pivot axes with respect to the neutral surface for  $R=900$  and 10000 mm, respectively. The results indicate a trend similar to that seen in the thickness sensitivity study, specifically, a larger variance in slope angle near the ends of the blade that is dependent on curvature. In this case the curvature dependence is less pronounced.

Sensitivity studies of the pivot-to-pivot distance showed that variations of order  $\pm 125 \mu\text{m}$  had a negligible affect on focal aberration.

These numerical results show that, while the functional form of  $\varepsilon_v$  can be highly sensitive to small geometric inaccuracies, the slope error is still well below  $0.15^\circ$ ; hence, it should be possible to construct a blade that meets the desired focal performance. Certainly, other factors not modeled here such as the free-standing flatness of the blade, geometric symmetry and crystal mounting will have an effect on the vertical aberration as well.

<sup>1</sup> This endurance limit is based on  $5 \times 10^8$  cycles of completely reversed stress.

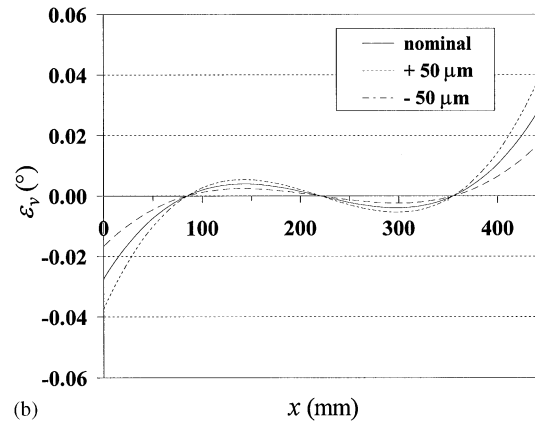
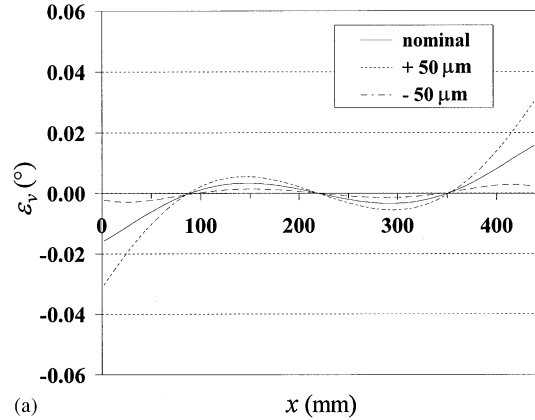
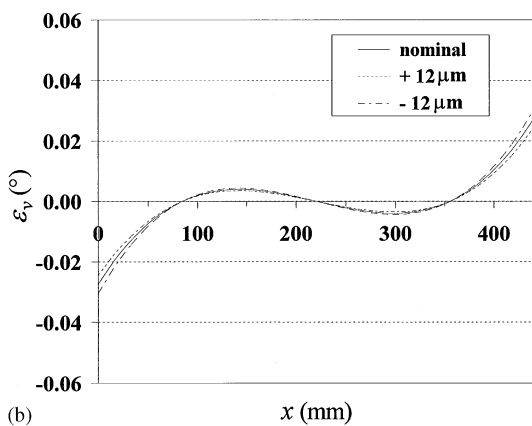
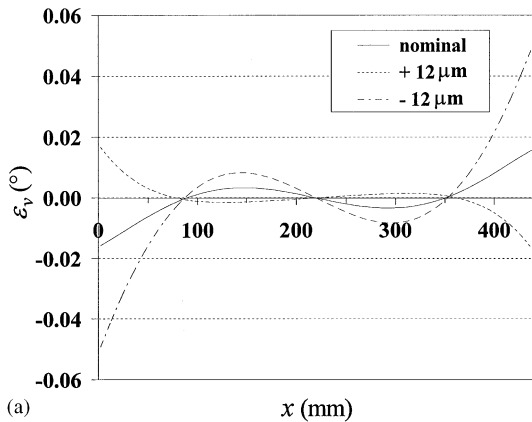


Fig. 8. Vertical aberration in a blade buckled to (a)  $R=900$  mm and (b)  $R=10000$  mm as a function of thickness variation. Curves represent the slope error for a blade with the nominal thickness profile given by Eq. (19), as well as for  $\pm 12 \mu\text{m}$  uniform deviations from the nominal dimensions.

Fig. 9. Vertical aberration in a blade buckled to (a)  $R=900$  mm and (b)  $R=10000$  mm as a function of the distance from the pivot to the neutral surface. Curves represent the slope error in a blade with the pivot nominally located on the neutral surface, as well as  $\pm 50 \mu\text{m}$  from the neutral surface.

Collectively, these additional factors, along with the horizontal aberration,  $\varepsilon_h$ , are considered in the experimental studies that follow.

#### 4. Experimental results/discussion

Two blades were fabricated from stress relieved 6061-T6 aluminum using Electrical Discharge Machining (EDM) on a Charmilles Robofill 300 wire machine. Using the multi-stage fabrication process developed here, the blades were produced with a thickness accuracy of  $\pm 12 \mu\text{m}$ , and the symmetry between the right ( $0 \leq s \leq S$ ) and left ( $S \leq s \leq 2S$ ) halves differed by less than  $10 \mu\text{m}$ . The

flatness of the freestanding blades was held to within  $0.15$  mm.

Electromechanical and optical measurement techniques were used to characterize the focal performance of each blade and determine the validity of the numerical analysis presented above. To perform these tests, a test-cell was constructed to buckle the blades by controlled displacement of one pivot axis. The test-cell accommodates up to three blades and when completely populated mimics a doubly focusing monochromator, see Fig. 10. Mechanical adjustments facilitate radius calibration so that each blade buckles to approximately the same curvature for a given pivot displacement.

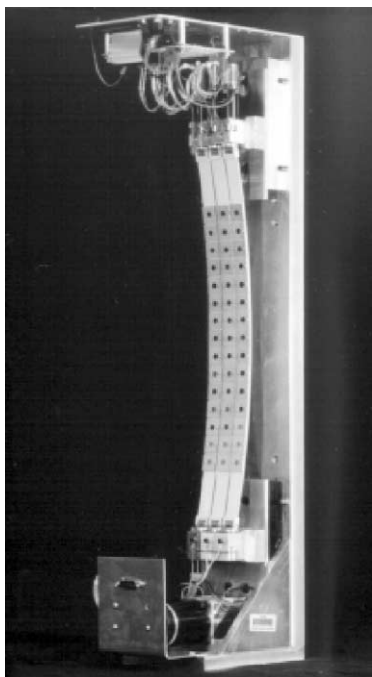


Fig. 10. Photograph of the blade test-cell in the optical test configuration. Here, the blades are populated with 15 mirrored platelets and buckled to a radius of 900 mm. The test-cell mimics a doubly focusing monochromator; vertical focus is achieved by fixed displacement of the lower pivot axes, horizontal focus is achieved by independent rotation of each blade.

Each blade was serialized and tested to determine the relative focal performance of each blade. Detailed measurements were taken on the two blades representing the best and worst focal performance of the four; SN102300003 and SN102300002, respectively. The remainder of this section describes the tests performed and the results obtained. Results given are for blades SN102300002 and SN102300003.

#### 4.1. Deflection curves

Deflection curves were measured for pivot displacements corresponding, approximately, to the same three radii modeled numerically:  $R=900$ , 2500 and 10 000 mm. Measurements were taken on the flat surface of the blade in 1.25 mm increments using a Mitutoyo BHN710 Coordinate Measuring

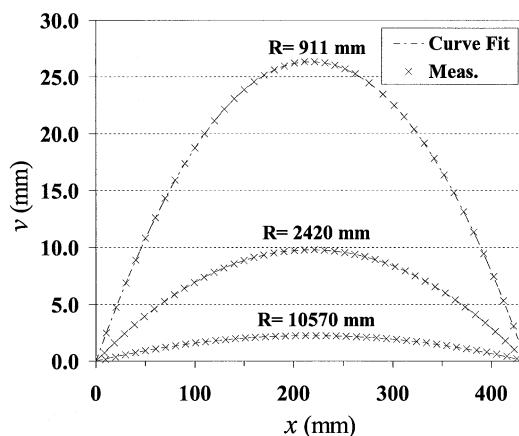


Fig. 11. Measured deflection of blade SN102300003 and the corresponding curve fit for three radii:  $R=911$ , 2420, 10 570 mm. Only a sparse number of measured points are shown for clarity. Measurement uncertainty is  $\pm 10 \mu\text{m}$ .

Machine (CMM) at the National Institute of Standards and Technology, Gaithersburg, MD.

Fig. 11 shows the measured data for SN102300003 along with best-fit circular deflection curves. The maximum and RMS deviation of the measured deflections with respect to the best-fit curves are tabulated in Table 2 for SN102300002 and SN102300003 along with corresponding numerical predictions. Given measurement error and geometric variances in the blades, the data are in reasonable agreement with the numerical prediction.

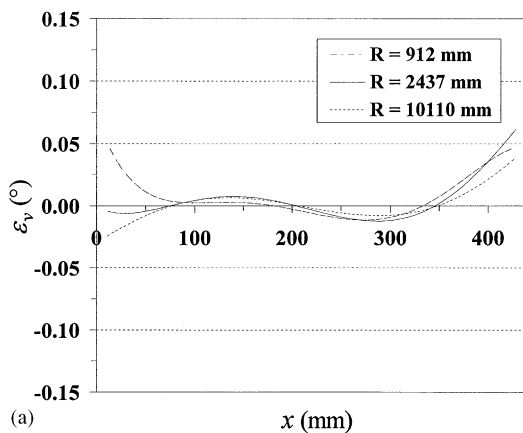
#### 4.2. Vertical aberration—blade only

The vertical aberration  $\varepsilon_v$  has been characterized using the deflection measurements obtained with the CMM. To filter random measurement errors, a polynomial fit to the measured data was used as the basis for calculating the slope of the deflection curve; care has been taken in selecting the order of the polynomial to ensure that measured data do not deviate from the polynomial fit by more than measurement error. The aberration is determined by comparing the slope angle of the deflection curve (polynomial fit) to the slope angle of the circular arc that best fits the measured data.

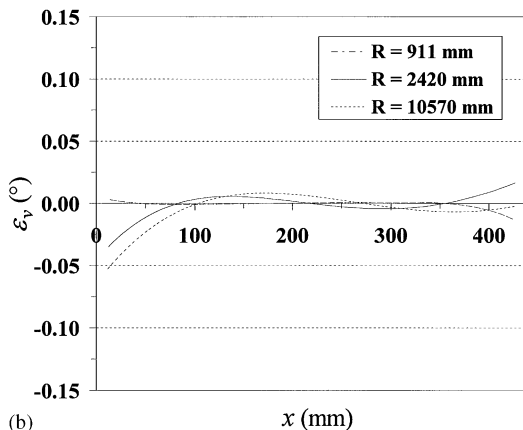
Table 2

Deflection statistics for SN102300002 and SN102300003 with respect to best-fit circular curves<sup>a</sup>

SN102300002			SN102300003		
R (mm)	Deviation ( $\mu\text{m}$ )		R (mm)	Deviation ( $\mu\text{m}$ )	
	max	rms		max	rms
912	24	8	911	10	2
	[5.0]	[2.0]		[5.0]	[2.0]
2437	27	7	2420	23	4
	[8.6]	[3.1]		[8.6]	[3.1]
10110	15	5	10570	35	7
	[7.1]	[2.5]		[7.1]	[2.5]

<sup>a</sup>The data in brackets represent the numerical prediction. Measurement uncertainty is  $\pm 10 \mu\text{m}$ .

(a)



(b)

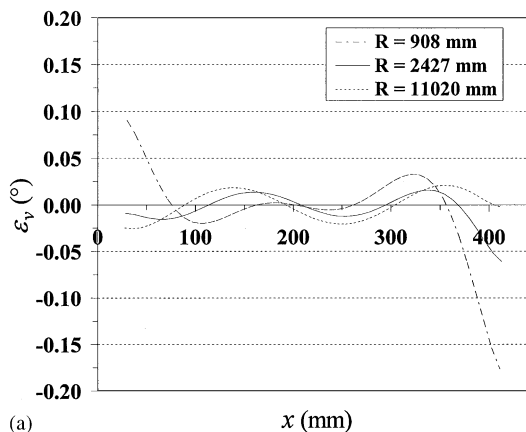
Fig. 12. Vertical aberration in (a) SN102300002 for three radii:  $R=912$ , 2437 and 10110 mm, and (b) SN102300003 for three radii:  $R=911$ , 2420 and 10570 mm.

Figs. 12a and b show  $\varepsilon_v$  for SN102300002 and SN102300003, respectively. For both blades  $\varepsilon_v$  is less than  $0.075^\circ$  and, as predicted, the dependence on radius of curvature is negligible. In general, these results are in excellent agreement with numerical prediction, particularly given the sensitivity to geometric variances. This data confirms that it is possible to construct an elastic focusing element that conforms to the shape of an arc of constant radius over a wide range of radii with minimal slope error.

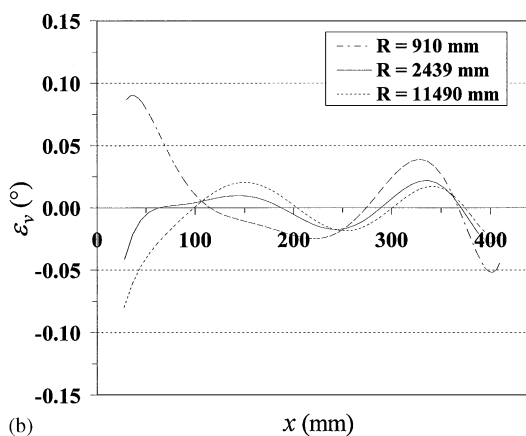
#### 4.3. Vertical aberration—blade w/19 crystals

The effect of mounting crystals has been investigated by taking measurements of the deflection curve with simulated crystals mounted to the blade. These aluminum platelets have the same dimensions as the crystals except the height is reduced from 20 to 10 mm leaving a 10 mm gap between platelets, sufficient to probe the front surface of the blade with the CMM. Shims,  $19 \text{ mm} \times 5 \text{ mm} \times 0.25 \text{ mm}$ , placed between the platelets and the blade surface enable unrestricted bending. Deflection curves were measured with nineteen simulated crystals mounted to the blade and the vertical aberration  $\varepsilon_v$  was determined using the method described above.

The vertical aberration  $\varepsilon_v$  for SN102300002 and SN102300003, fully populated with simulated crystals, is shown in Figs. 13a and b, respectively.



(a)



(b)

Fig. 13. Vertical aberration in (a) SN102300002 and (b) SN102300003 with 19 simulated crystals mounted to the flat side of the blade. 0.25 mm thick  $\times$  5 mm wide shims between the crystals and the blade surface enable unrestricted bending.

It is evident from these plots and the previous results that mounting crystals to the blade increases the vertical aberration. This effect stems from localized stiffening in regions where the shims contact the blade and is most pronounced at the ends where the gradient in blade thickness is large. The slope error is greatest for large curvatures and, at one end of SN102300002, slightly exceeds the desired  $0.15^\circ$  limit for  $R \approx 900$  mm. However, in general,  $\varepsilon_v(R, s)$  is less than  $0.15^\circ$ . For SN102300003,  $\varepsilon_v(R, s)$  is less than  $0.1^\circ$  over the entire domain. The same holds true for 17 of 19 crystal locations on SN102300002; only one exceeds the  $0.15^\circ$  limit.

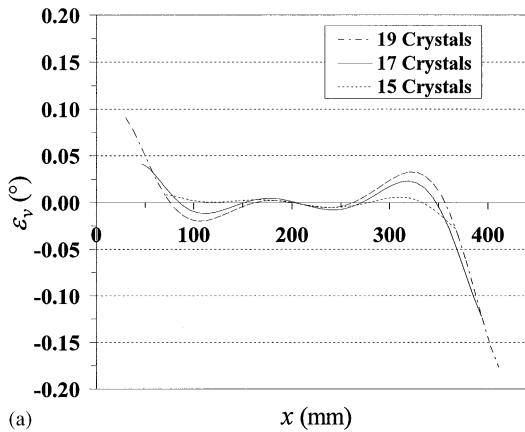
#### 4.4. Vertical aberration—blade w/15, 17 and 19 crystals

The fact that  $\varepsilon_v$  is largest near the ends of the blade naturally leads to the consideration that it may be possible to reduce the overall slope error if the blade is only sparsely populated with crystals, i.e. the end crystals are removed. From a practical perspective, this concept has merit. It will often be the case that it is desirable to locate extraneous hardware some reasonable distance from the clear aperture of the neutron beam to limit parasitic scattering. Therefore, for most practical implementations, the blade will be longer than physically necessary to mount the required number of crystals. This is the case for the application here where only 15 crystals per blade are required, though 19 crystals can be accommodated.

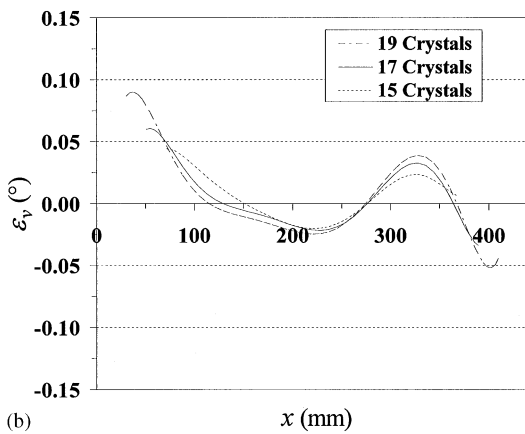
Figs. 14a and b show  $\varepsilon_v$  for SN102300002 and SN102300003, respectively, buckled to  $R=900$  mm for three different populations of crystals: 15, 17 and 19. The maximum and RMS values for  $\varepsilon_v$  are tabulated in Table 3. It is clear from the data that eliminating crystals near the ends of the blade reduces the vertical aberration considerably. The change is most notable in the case of SN102300002 where  $\varepsilon_v$  is reduced by a factor of six for a decrease in the number of crystals from 19–15. With 15 crystals  $\varepsilon_v$  is less than  $0.05^\circ$  for both blades.

#### 4.5. Horizontal and vertical aberration—optical characterization

Optical imaging studies have been conducted to determine the horizontal aberration  $\varepsilon_h$  and to verify the vertical aberration results reported above. Optical methods are well suited for this purpose since the geometry of neutron Bragg reflection is similar to specular reflection of light. For this test, polished aluminum platelets were used in lieu of crystals, see Fig. 10. The circular polished region is confined to the center of the platelet. A white point source and imaging screen were positioned one focal length away from the blade. The curvature of the blade was adjusted until the individual spots from each mirrored platelet converged to a minimized spot on the



(a)



(b)

Fig. 14. Vertical aberration in (a) SN102300002 and (b) SN102300003 buckled to  $R=900$  mm for three different populations of crystals: 15, 17 and 19. The aberration is only plotted for the region occupied by crystals.

imaging screen. For each platelet, the wedge angle between the mirrored surface and the back mounting surface was characterized to determine the zero-aberration image size of the multi-crystal spot. The aberration was then determined from the difference between the minimized and zero-aberration spot sizes.

Three-sigma spot sizes were measured for six focal lengths in the range  $900 \text{ mm} < R < 10\,000 \text{ mm}$ . For crystal populations of 15, 17, and 19, the maximum horizontal and vertical aberrations were determined to be less than  $0.15^\circ$ . Comparison of spot sizes for different blade

Table 3

Slope error for SN102300002 and SN102300003 buckled to  $R=900$  mm with 15, 17 and 19 simulated crystals mounted to the flat side of the blade

No. crystals	SN102300002		SN102300003	
	Slope error ( $^\circ$ )		Slope error ( $^\circ$ )	
	max	rms	max	rms
19	0.176	0.036	0.090	0.021
17	0.126	0.023	0.059	0.015
15	0.030	0.005	0.047	0.011

populations showed negligible change in the vertical direction. This is somewhat contradictory to the data shown in Table 3. However, a detailed look at the wedge error of each platelet showed the error to be of the same order as the vertical aberration. Furthermore, the wedge error in crystals removed from the ends of the blade was small, statistically, compared to the remaining crystals, which explains the negligible change in spot size. In the horizontal direction, the spot size of SN102300003 increased by  $\sim 0.03^\circ$  for  $R \geq 3800$  mm when increasing the crystal population from 17 to 19; no change was detected between crystal counts of 15 and 17. Crystal population had no effect on the horizontal aberration for SN102300002.

#### 4.6. Fatigue life

Lifecycle studies were conducted to test for blade fatigue and wear in the pivot hardware. Variations in spot size were tracked over many focus cycles using the optical arrangement described above. The radius of curvature was cycled between 7000 and 900 mm. Changes in spot size were noted at the 7000 mm position. Initially, a large change in focus was discovered after several hundred cycles. This was due to a temperature rise in the test-cell structure caused by heat from the vertical focus stepper motor. For the purposes of testing, a fan was implemented to remove the heat and further testing showed negligible change in focus. More than five thousand vertical focus

cycles were completed with no signs of mechanical wear or fatigue. This test showed that, for large radii, the radius of curvature could be quite sensitive to the local thermal environment. In practice though, focus adjustments happen over short timescales, not continuously as was the case here, and, provided motor hold currents are minimized, thermal changes should be inconsequential. Additionally, an active control system could be implemented to maintain focus if needed.

## 5. Summary

A low mass elastic mechanism for the vertical focusing of neutrons has been presented. The theoretical derivation has been given for the variable thickness profile that enables the thin blade device to buckle to an arc of constant radius over a wide range of radii. Subsequent numerical analysis demonstrated its potential performance. Four blades were fabricated and the deviation in the buckled profile with respect to an arc of constant radius for each blade was characterized experimentally. These results were consistent with numerical prediction. Further studies were performed to characterize the performance of the blade with crystals mounted to it. Electro-mechanical and optical metrology showed that, for the focal range  $900 \text{ mm} < R < 10\,000 \text{ mm}$ , the maximum vertical aberration in a blade with crystals occupying 90% of the length is of order  $0.15^\circ$ ; the maximum occurring at  $R = 900 \text{ mm}$ . It was also shown that this maximum is reduced considerably if crystals are restricted to the central 70% of the blade. Horizontal aberration was characterized optically and determined to be less than  $0.15^\circ$  over the same focal range, with a slight sensitivity to crystal population at large radii. Additional studies were performed to look for signs of blade fatigue or wear in the pivot hardware. After more than five thousand vertical focus cycles no anomalies were discovered.

## 6. Conclusion

An elastic focusing mechanism has been presented that is ideal for use in doubly focusing monochromators. The device is simple, contains no moving parts, has zero backlash and can place a one-dimensional array of diffracting crystals on an arc of constant radius to better than  $0.15^\circ$  over a wide range of radii. In addition, the scalability of the design enables the construction of arrays ranging in size from tens to hundreds of individual crystals. Finally, the inherently low mass of the device and its single component nature, which eliminates the need for highly scattering materials, promises a significant reduction in background compared to traditional focusing mechanisms. Combined, these merits facilitate the construction of very high signal-to-noise spectroscopic systems, which in turn will contribute to advances in the scientific understanding of many materials as well as a better understanding of the underlying physics.

## Acknowledgements

The authors would like to thank Mr. Wendell Combs, Mr. Joe Orndorff and Mr. Gregory A. Scharfstein for their assistance with the metrology efforts that were so vital to this work. Work at JHU was supported in part by the National Science Foundation through DMR-0074571.

## References

- [1] T. Riste, Nucl. Instr. and Meth. A 86 (1970) 1.
- [2] C.L. Broholm, Nucl. Instr. and Meth. A 369 (1996) 169.
- [3] R.E. Lechner, R.v. Wallpach, H.A. Graf, F.-J. Kasper, L. Mokrani, Nucl. Instr. and Meth. A 338 (1994) 65.
- [4] W. Bühner, Nucl. Instr. and Meth. A 338 (1994) 44–52.
- [5] M. Popovici, K.W. Herwig, R. Berliner, W.B. Yelon, L. Groza, Physica B 241 (1997) 216–218.
- [6] J.M. Gere, S.P. Timoshenko, Mechanics of Materials, 1990, pp. 601, 462–463.
- [7] Byron D. Tapley, Eshbach's Handbook of Engineering Fundamentals, 1990, p. 16.85.